







Stability of the interorbital-hopping mechanism for ferromagnetism in multi-orbital Hubbard models

Ling-Fang Lin ^{1✉}, Yang Zhang ^{1✉}, Gonzalo Alvarez², Michael A. McGuire ³, Andrew F. May ³,
Adriana Moreo ^{1,3} & Elbio Dagotto ^{1,3}

The emergence of insulating ferromagnetic phase in iron oxychalcogenide chain system has been recently argued to be originated by *interorbital* hopping mechanism. However, the practical conditions for the stability of such mechanism still prevents the observation of ferromagnetic in many materials. Here, we study the stability range of such ferromagnetic phase under modifications in the crystal fields and electronic correlation strength, constructing a theoretical phase diagram. We find a rich emergence of phases, including a ferromagnetic Mott insulator, a ferromagnetic orbital-selective Mott phase, together with antiferromagnetic and ferromagnetic metallic states. We characterize the stability of the ferromagnetic regime in both the Mott insulator and the ferromagnetic orbital-selective Mott phase forms. We identify a *large* stability range in the phase diagram at both intermediate and strong electronic correlations, demonstrating the capability of the interorbital hopping mechanism in stabilizing ferromagnetic insulators. Our results may enable additional design strategies to expand the relatively small family of known ferromagnetic insulators.

¹Department of Physics and Astronomy, University of Tennessee, Knoxville, TN 37996, USA. ²Computational Sciences & Engineering Division and Center for Nanophase Materials Sciences, Oak Ridge National Laboratory, Oak Ridge, TN 37831, USA. ³Materials Science and Technology Division, Oak Ridge National Laboratory, Oak Ridge, TN 37831, USA. ✉email: lfliin@utk.edu; yizhang@utk.edu

Transition metal (TM) systems involving multi-orbital correlated electrons continue attracting much attention due to their rich physical properties^{1–6}. In the standard Hubbard Hamiltonian of a multiorbital system, the interplay of the elements of the hopping matrix, the crystal fields Δ splitting orbitals, the Hubbard repulsion U , and the Hund coupling J_H linking all orbitals, often leads to several intriguing electronic phases arising from their competition, such as the molecular-orbital state in dimers⁵, the spin-singlet state^{7,8}, various forms of orbital ordering^{9,10}, and the recently much-addressed orbital-selective physics^{11–16}. An attractive example of orbital-selective states is the unusual orbital-selective Mott phase (OSMP) (Fig. 1a), involving a mixture of localized and itinerant behavior of the different orbitals when in the *intermediate* electronic correlation region^{17–21}.

It is precisely the intermediate coupling regime that harbors the most surprises because in this region hand-waving lines of reasoning are often not trustworthy since many couplings are similar in magnitude and reliable predictions are difficult, unless involving robust computational methodologies. This is the true regime of “complexity” in correlated electrons, where the expression complexity is used as denoting the emergence of unexpected properties from seemingly simple local interactions. This intermediate region will be the focus of this work.

Before moving into the focus of present contribution, we wish to briefly remind the reader of the practical importance of enlarging the family of ferromagnetic (FM) or ferrimagnetic insulators. Materials with these properties have important applications in the field of spintronics, where their low magnon damping and ability to exchange couple magnetism into neighboring materials are particularly useful^{22–24}. Compared to anti-ferromagnetic (AFM) insulators, FM insulators are relatively rare, particularly among oxides^{25–27}. Ferrimagnetic ferrite garnets like $\text{Y}_3\text{Fe}_5\text{O}_{12}$ (yttrium iron garnet, or YIG) are commonly used in devices; however, some limitations of these materials have been noted and development of alternatives is an active and important area of research²⁸. Perhaps the earliest recognized example of a FM insulator was CrBr_3 ²⁹. The combination of FM order and cleavability has made this compound, its analogue CrI_3 , and the related compounds CrSiTe_3 and CrGeTe_3 important materials in the field of functional van der Waals heterostructures^{24,30,31}. Although ferromagnetism is usually associated with TMs, several rare-earth-based FM insulators are also known, including the rock-salt structure compounds EuO , EuS , and mononitrides of several rare earth elements^{32,33}. Hexagonal ferrites and spinels such as CoFe_2O_4 ^{34,35} are also of interest²⁸. FM semiconducting behavior has also been reported in spinel chalcogenides like CdCr_2S_4 and CrCr_2Se_4 ^{27,36}.

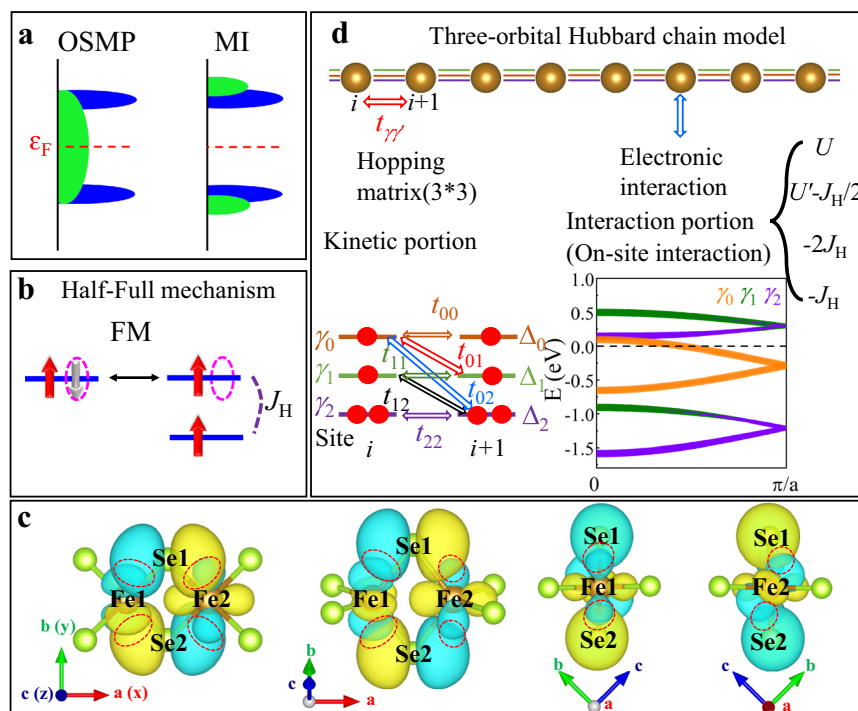


Fig. 1 Orbital-selective Mott phase, the half-full mechanism, and model Hamiltonian. **a** Sketch of the local density-of-states for the orbital-selective Mott phase (OSMP) and Mott insulator (MI) phases, in a multi-orbital system with electronic correlations. Here we use two electrons in two orbitals per site, as example. For the OSMP, one orbital forms a Mott state with a gap, while the other orbital remains itinerant and gapless, leading to a globally metallic phase. For the MI state, both orbitals form Mott states, resulting in an insulating phase. **b** Sketch of the FM superexchange mechanism discussed in ref. 39 induced by the large entanglements between doubly occupied and half-filled orbitals. The half-filled orbitals are coupled by Hund’s coupling J_H . Orbitals are indicated by blue lines. Electrons with spin up or down are indicated by red or gray arrows, respectively. The two-way thin arrows indicate the overlap between inter-site orbitals. The virtual hopping process is highlighted by the red dashed ovals. **c** The effective Wannier functions (WF) of orbital γ_1 (d_{yz}) for Fe1 and γ_2 ($d_{x^2-y^2}$) for Fe2 with bridges using the Se1 and Se2 p_x orbitals. The robust overlap between these WFs, which is related to the amplitude of hoppings t_{12} , are indicated by the dashed red ovals. Isosurface is set to be 3 here. Different colors represent different signs of the WF. The Wannier function plot is produced using WANNIER90 code⁴² and VESTA⁶⁵. **d** The three-orbital Hubbard model on a one-dimensional chain lattice geometry used in our study, including the kinetic component and electronic interaction. $t_{\gamma\gamma'}$ represents hopping from orbital γ to orbital γ' between nearest neighbor sites i and $i + 1$. Crystal-field splittings are labeled by $\Delta_{0,1/2}$. Orbitals are marked by $\gamma_{0,1/2}$. Hubbard repulsion U , U' between electrons at different orbitals, Hund’s coupling J_H , and the inter-orbital electron-pair hopping terms are also list, more details can be found in Model Hamiltonian part. Inset: The non-interacting band structure along the chain direction using the original parameters from ref. 39.

Consider now the primary specific goal of this publication. Most TM insulating materials are AFM while few display FM order. This can be understood from the simplicity and robustness of Anderson's superexchange AFM theory which is based on second-order perturbation theory in the hopping amplitudes^{37,38}. However, recently a "half-full" mechanism involving large entanglements between doubly occupied and half-filled orbitals was proposed³⁹ to understand the puzzling origin of FM order along the chain direction in $\text{Ce}_2\text{O}_2\text{FeSe}_2$ ^{40,41}, as shown in Fig. 1b. Note that we employ the word "entanglement" between orbitals with different electronic population as indicating that in a quantum description these orbitals cannot be considered as independent of one another, but they are intrinsically coupled and this interplay of two orbitals with different electronic populations is at the heart of the *interorbital* hopping mechanism proposed.

Specifically, based on second-order perturbation theory in the hopping amplitudes, the total gain in energy of the FM configuration due to the robust hopping t_{12} between half-occupied and fully occupied orbitals was found to be:

$$\Delta E_{\text{FM}} = -\frac{|t_{12}|^2}{U - 3J_{\text{H}} + \Delta}. \quad (1)$$

where $\Delta = \Delta_1 - \Delta_2$ is the crystal-field splitting between the half-filled and double-occupied orbitals. On the other hand, in the AFM state the total energy gained from t_{12} is

$$\Delta E_{\text{AFM}} = -\frac{|t_{12}|^2}{U - J_{\text{H}} + \Delta}. \quad (2)$$

Hence, the interorbital electronic hopping t_{12} by itself favors a FM interaction, basically driven by the Hund coupling. However, the prevailing intra-orbital hoppings t_{11} or t_{22} favor a superexchange AFM state with gains in energy such as $\Delta E \sim -\frac{|t_{11}|^2}{U+J_{\text{H}}}$. More details of analysis of second-order perturbation theory can be found in Supplementary Note II.

Then, the dominant magnetic order of the material under consideration is decided by the competition of these different channels. Our previous work showed that in some cases, the hopping t_{12} can be large enough to stabilize a FM insulating phase, without the need to resort to the more frequently mentioned mechanism of double exchange, which produces robust FM but with metallic character, and the nearly 90° bonds, typically associated with low critical temperatures. It is also worth remarking that while our previous theoretical work, as well as the present contribution, are in one dimension, the simple second-order perturbative foundations of the FM phase are robust and valid in higher dimensions as well.

To intuitively understand the effective interorbital hopping t_{12} between the Fe1 d_{yz} and Fe2 $d_{x^2-y^2}$ orbitals, it is crucial to include Se's p orbitals in the Wannier90 calculations⁴². By comparing all channels contributing to t_{12} , we found out that the dominant channel occurs when the Se's p_x orbital acts as a "bridge" between the $3d$ orbitals. To have an intuitive visual view of t_{12} , the WFs related to this p_x channel are shown in Fig. 1c. In this sketch, the bending of the Fe-Se-Fe bond is important to achieve a nonzero t_{12} matrix element.

While this mechanism has been observed for fixed hopping and crystal fields³⁹, some questions naturally arise on its stability and transferability to other materials. How does the FM state induced by this half-full mechanism evolve by varying the crystal-field values as well as the strength of the electronic correlations? At intermediate couplings, could the OSMP with FM order be instead stable in this half-full system with crystal field effects? What other magnetic or electronic phases can emerge by considering the competition of those parameters in an extended

phase diagram? In other words, are the previous results³⁹ an anomaly or truly indicative of a general mechanism?

To address these broad goals, we investigated the crystal field and electronic correlations effects on the half-full FM ground state previously reported, by using the density matrix renormalization group (DMRG) technique on the multi-orbital Hubbard model. Fixing the Hund coupling to $J_{\text{H}}/U = 0.25$, realistic for materials of the iron family⁴, the magnetic and electronic phase diagram was theoretically constructed varying Δ and U/W . One of our main results is that the FM phase is stable in a large portion of the phase diagram. Namely, the previously reported FM phase due to a robust interhopping amplitude t_{12} is here shown not to be fragile, as often spin liquid states tend to be, but representative of broad tendencies that until now were not considered by the community of experts. Specifically, we found both the recently discovered FM Mott insulator (MI) and the FM OSMP phases are stable at intermediate and strong electronic correlation, respectively. Our results potentially open a vast avenue of research and the possibility for the family of FM insulators to be considerably enlarged. We propose that via ab-initio techniques, a systematic exploration of materials with robust interorbital hopping could provide the first steps toward additional FM insulators in the near future.

In addition, several other magnetic electronic phases are also revealed in our study arising from the competition of hopping, crystal field splitting, and electronic correlations, involving an AFM2 metal (i.e. an AFM state with blocks of size 2), a FM metallic state, and staggered canonical AFM1 MI phases. This exemplifies the complexity that emerges from multiorbital models when they are analyzed with reliable computational techniques, particularly in the challenging intermediate coupling regime.

Results

Model Hamiltonian. In this work, as an example of our broad ideas, we employ a canonical three-orbital Hubbard model defined on a one-dimensional (1D) chain lattice, including the kinetic energy and interaction terms written as $H = H_{\text{k}} + H_{\text{int}}$. The tight-binding kinetic component is

$$H_{\text{k}} = \sum_{i\sigma} t_{\gamma\gamma'}^{\vec{\alpha}} \left(c_{i\sigma\gamma}^\dagger c_{i+\vec{\alpha}\sigma\gamma'} + H.c. \right) + \sum_{i\gamma\sigma} \Delta_\gamma n_{i\gamma\sigma}, \quad (3)$$

where the first term represents the hopping of an electron from orbital γ at site i to orbital γ' at the nearest neighbor site $i + \vec{\alpha}$. $c_{i\sigma\gamma}^\dagger (c_{i\sigma\gamma})$ is the standard creation (annihilation) operator, γ and γ' represent the different orbitals, and σ is the z -axis spin projection. Δ_γ represent the crystal-field splitting of each orbital γ .

The electronic interaction portion of the Hamiltonian includes the standard intraorbital Hubbard repulsion U , the electronic repulsion U' between electrons at different orbitals, the Hund's coupling J_{H} , and the on-site inter-orbital electron-pair hopping terms. Formally, it is given by:

$$H_{\text{int}} = U \sum_{i\gamma} n_{i\uparrow\gamma} n_{i\downarrow\gamma} + (U' - \frac{J_{\text{H}}}{2}) \sum_i n_{i\gamma} n_{i\gamma'} - 2J_{\text{H}} \sum_i \mathbf{S}_{i,\gamma} \cdot \mathbf{S}_{i,\gamma'} + J_{\text{H}} \sum_i \left(P_{i\gamma}^\dagger P_{i\gamma'} + H.c. \right), \quad (4)$$

where the standard relation $U' = U - 2J_{\text{H}}$ is assumed and $P_{i\gamma} = c_{i\downarrow\gamma} c_{i\uparrow\gamma}$.

Specifically, here we consider a three-orbital Hubbard model with four electrons per site (see the sketch in Fig. 1d), where the

crystal-field splitting and hopping matrix are adopted from the real iron chain $\text{Ce}_2\text{O}_2\text{FeSe}_2$ system as a concrete example³⁹. To study the crystal-field splitting effects between half-filled and fully occupied orbitals we fixed the values of Δ_0 and Δ_1 as in³⁹ but vary Δ_2 , as well as U/W . In the “DMRG” portion of the methods section, the reader can find the specific 3×3 hopping matrix and values of Δ_0 and Δ_1 employed. Note that all the DMRG calculations are performed at temperature $T=0$.

Phase diagram with crystal field effects. First, using DMRG we constructed the general phase diagram varying the electronic correlations U/W and crystal field splitting Δ_2 , as shown in Fig. 2. Although the original model parameters are derived from the five d orbitals of the real iron chain materials $\text{Ce}_2\text{O}_2\text{FeSe}_2$, the main conclusions are not limited to this specific material or to three-orbital models, but expand to any other system with large inter-orbital hopping between half-filling and fully occupied orbitals. Our primary aim is to test the *interorbital* hopping driven FM mechanism beyond $\text{Ce}_2\text{O}_2\text{FeSe}_2$. This phase diagram is obtained from measurements of the spin-spin correlation $S(r)$, the site-average occupancy n_γ , and charge fluctuations δn_γ , all at J_H/U

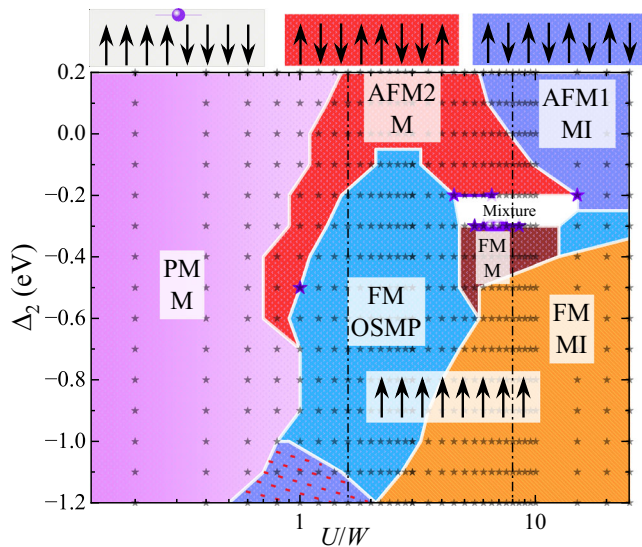


Fig. 2 DMRG phase diagram. Phase diagram of the three-orbital Hubbard model varying U/W and crystal-field splitting Δ_2 , using DMRG and an $L = 16$ chain system with open boundary conditions. Note that the three-orbital character of the problem renders this system equivalent to a challenging highly entangled 3×16 ladder lattice, with hoppings at fairly long distances such as between top and bottom legs in this effective 3×16 lattice. We use the prototypical value $J_H/U = 1/4$. Different electronic and magnetic phases are indicated by solid regions and labels, including paramagnetic metal (PM M, in pink), ferromagnetic orbital-selective Mott phase (FM OSMP, in light blue), ferromagnetic Mott insulator (FM MI, in yellow), antiferromagnetic1 Mott insulator (AFM1 MI, in purple), ferromagnetic metal (FM M, in maroon) and antiferromagnetic2 metal (AFM2 M, in red). Due to strong competition between opposite tendencies, some mixed phases, marked by purple stars, are found near the boundaries, especially around $\Delta_2 \sim -0.25$ eV and $U/W \sim 8$ (white region). The antiferromagnetic4 (AFM4) phase, marked by a purple circle, is also displayed in this region. Note that the boundaries should be considered only as crude approximations. We simply cannot have a very dense grid of points due to the high cost of DMRG. However, the existence of the six regions shown was clearly established by robust DMRG evidence near their centers, even if the boundaries are only crude estimations. All calculated data points are marked by gray stars. The two vertical dashed lines at $U/W = 1.6$ and 8.0 correspond to the results of Figs. 3 and 5.

$U = 0.25$ as already explained. The results are rich and include six different phases: (1) paramagnetic (PM) metallic (M) phase, (2) AFM2 M state, (3) FM OSMP, (4) AFM1 MI phase, (5) FM M state, and (6) FM MI phase. Note that in our case all the transitions between magnetic states are discontinuous in the order parameters, thus first order (with the caveat that we are in 1D thus the magnetic order is only quasi long-range order). The only exception is between a PM and ordered state: these tend to be smooth transitions.

At small electronic correlation ($U/W \lesssim 0.7$), the system displays PM behavior with three itinerant orbitals, where the spin correlation $S(r)$ involving two spin operators separated by a distance r decays rapidly with distance, as shown in Supplementary Note III. In this region, the hopping term plays the leading role, leading to the metallic behavior. At intermediate Hubbard coupling strength, the FM OSMP state—involving coexisting localized and itinerant electrons—is found to be stable in a large range of Δ_2 . Furthermore, two magnetic and electronic phases are also obtained in this intermediate region by changing Δ_2 . They are the AFM2 M and AFM1 MI phases, arising from the competition of Δ_2 and U/W . At large U/W , MI states with localized charges (n number of electrons either 1 or 2) dominate over a broad range of the crystal-field splitting Δ_2 . Also an FM M phase is found in a small region due to the competition of Δ_2 , U/W , and hopping amplitudes.

In this rich DMRG phase diagram, the FM phase is dominant in a large region of Δ_2 with the conduction type determined by the strength of the electronic correlations. At intermediate U/W , the system has simultaneously metallic and insulating orbitals, leading to the FM OSMP state. This OSMP is induced by the competition between hopping values of different orbitals and electronic correlations (Hubbard U , Hund coupling J_H): the electrons in the orbital with smaller hopping are *localized* at intermediate correlations U/W while the electrons in orbitals with larger hoppings remain *itinerant* i.e. metallic with non-integer filling. If we further increase the electronic correlations, the FM OSMP metallic state transitions to the FM MI phase where all three orbitals are fully Mott-localized at strong U/W . More details about Mott transition at $\Delta_2 \sim -0.8$ eV is discussed in Supplementary Note IV. By decreasing the crystal-field splitting Δ_2 towards zero, the FM state changes to different AFM phases because in this regime the canonical AFM superexchange mechanism dominates. Note that there is a small OSMP region at large U/W and $\Delta_2 \sim -0.3$ eV, where orbital $\gamma = 1$ is the localized one. This is slightly different from the large OSMP region at intermediate correlations, where orbital $\gamma = 0$ is the localized one. The reason is that, in the smaller OSMP region, Δ_2 is close to the crystal splitting value of orbital $\gamma = 0$, rendering stronger competition between orbital $\gamma = 0$ and $\gamma = 2$, while $\gamma = 1$ is easier to be localized.

FM-OSMP vs crystal field splitting. At intermediate Hubbard coupling strengths, the FM OSMP is found to be stable in a large region when decreasing Δ_2 into negative values (Fig. 2). Let us now focus on the crystal-field splitting effects at intermediate electronic correlation $U/W = 1.6$ in the phase diagram.

In the range -1.1 eV $\lesssim \Delta_2 \lesssim -0.2$ eV and at $U/W = 1.6$, the spin-spin correlation $S(r) = \langle \mathbf{S}_i \cdot \mathbf{S}_j \rangle$ vs r indicates FM order along the chain geometry (see the results at $\Delta_2 = -0.8$ and -0.4 eV in Fig. 3a). The distance is defined as $r = |i - j|$ with i and j site indexes. As shown in Fig. 3b, a sharp peak is also observed at $q = 0$ in the spin structure factor $S(q)$, clearly indicating FM order. In addition, the occupation of orbital $\gamma = 0$ is locked at the integer 1 in this region of Δ_2 , leading to the Mott-localized characteristic in this orbital, while the $\gamma = 1$ and $\gamma = 2$ orbitals

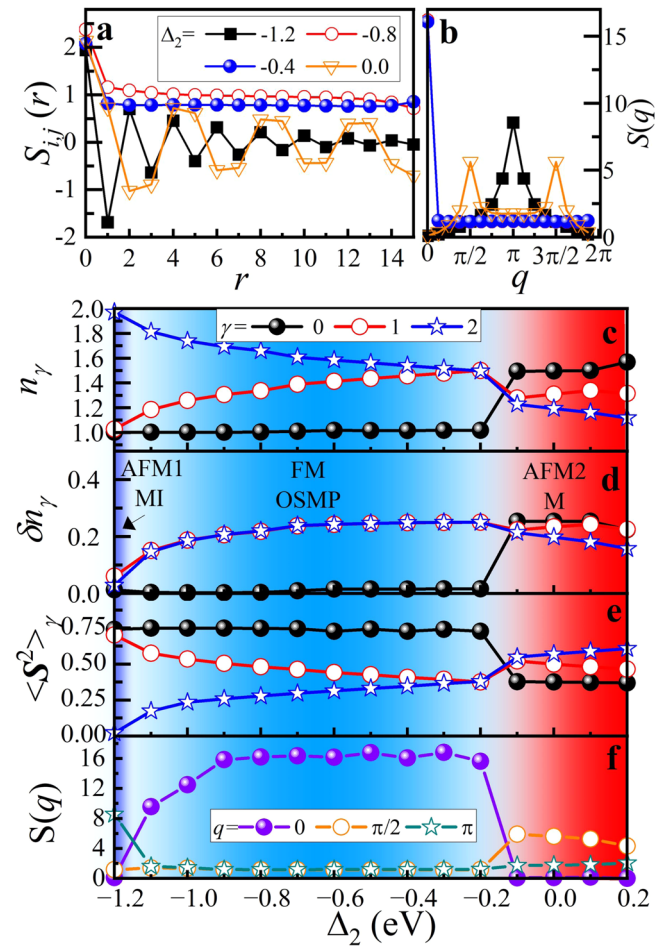


Fig. 3 Observables at intermediate correlation. **a** Spin-spin correlation $S(r) = \langle \mathbf{S}_i \cdot \mathbf{S}_j \rangle$ (with $r = |i - j|$ in real space) and **b** the spin structure factor $S(q)$, at different values of Δ_2 , all at $J_{\parallel}/U = 0.25$ and $U/W = 1.6$. **c** Orbital-resolved occupation number n_{γ} . **d** Charge fluctuations $\delta n_{\gamma} = \frac{1}{L} \sum_i (n_{i,\gamma}^2 - n_{i,\gamma})$. **e** Averaged value of the total spin-squared $\langle S^2 \rangle$, vs. Δ_2 , at $J_{\parallel}/U = 0.25$ and $U/W = 1.6$. **f** The spin structure $S(q)$ at $q = 0, \pi/2$, and π as a function of Δ_2 . (c-f) Different electronic and magnetic phases are marked by solid regions and labels, including antiferromagnetic1 Mott insulator (AFM1 MI, in purple), ferromagnetic orbital-selective Mott phase (FM OSMP, in light blue), and antiferromagnetic2 metal (AFM2 M, in red). For all these results, the chain length is $L = 16$ and DMRG was used.

have non-integer electronic densities, indicating metallic behavior, as displayed in Fig. 3c. To better understand the characteristics of the metallic vs. insulating behavior in different orbitals, we also studied the charge fluctuations δn_{γ} for different orbitals, as displayed in Fig. 3d. In the region ($-1.1 \text{ eV} \lesssim \Delta_2 \lesssim -0.2 \text{ eV}$), the $\gamma = 1$ and $\gamma = 2$ orbitals have some charge fluctuations because of the itinerant nature of their electrons. However, the charge fluctuation of $\gamma = 0$ is basically zero due to its localized orbital characteristics. Furthermore, $\langle S^2 \rangle_0$ saturates at $3/4$, corresponding to a half-filled orbital with spin $1/2$ at each site, while $\langle S^2 \rangle_1$ and $\langle S^2 \rangle_2$ are less than $3/4$, as shown in Fig. 3e. Thus, the system displays the orbital selective Mott characteristics with one localized orbital ($\gamma = 0$) and two itinerant orbitals ($\gamma = 1$ and $\gamma = 2$) and with global FM order.

Decreasing further Δ_2 ($\lesssim -1.1 \text{ eV}$), the system displays the canonical staggered AFM phase with the $\uparrow\downarrow\uparrow\downarrow$ configuration unveiled by $S(r)$, while the spin structure factor $S(q)$ shows also a sharp peak at $q = \pi$ (see results for $\Delta_2 = -1.2 \text{ eV}$ in Fig. 3b). Moreover, all three orbitals are integer occupied ($n_0 = 1, n_1 = 1,$

and $n_2 = 2$) in this state. Furthermore, $\langle S^2 \rangle_0$ and $\langle S^2 \rangle_1$ saturates at $3/4$, corresponding to the half-filled orbital, while $\langle S^2 \rangle_2$ is zero, indicating a double-occupied orbital, as shown in Fig. 3e. Hence, the system is in an AFM1 MI state in this region of Δ_2 . Because $\Delta = \Delta_1 - \Delta_2$ is larger than the Hund coupling J_H , the extra electrons prefer to stay in the $\gamma = 2$ orbital even with a large interorbital hopping t_{12} . In this case, the system can be effectively regarded as a two-half-occupied orbital system, where the intraorbital hoppings lead to the Heisenberg AFM coupling, resulting in the expected AFM1 phase characteristic of one-orbital Hubbard U models, where the Anderson superexchange prevails.

As an extra clarification, the small AFM1 MI region at around $\Delta_2 \lesssim -1.1 \text{ eV}$ and $U/W \sim 1$, alternatively, may be a Slater insulator (purple with red dashed lines). Clearly, between the weak coupling limit that harbors the Slater insulator and the strong coupling limit where the Mott insulator is located, there is a complex crossover region with features common to both³. The most strict way to distinguish Mott vs Slater is to study the insulating vs metal characteristics, respectively, above the magnetic ordering temperatures. But performing DMRG at a finite temperature for a multiorbital model is beyond our computational resources. Moreover, in 1D a sharp magnetic critical temperature is not expected. In the multi-orbital model, this open question is worthy of more detailed investigations in the future.

Increasing Δ_2 , the AFM tendency also increases, leading to competition with the FM tendency, resulting in more unusual phases. When $\Delta_2 > -0.2 \text{ eV}$, the spin-spin correlation $S(r)$ at $\Delta_2 = 0.0 \text{ eV}$ shows clearly the formation of antiferromagnetically coupled FM spin clusters with a $\uparrow\uparrow\downarrow\downarrow$ AFM2 pattern, as shown in Fig. 3a. Furthermore, the spin structure factor $S(q)$ also displays a sharp peak at $q = \pi/2$, corresponding to the AFM2 phase, as shown in Fig. 3b. Moreover, the four electrons per site are in non-integer orbitals with large charge fluctuations, indicating metallic behavior (Figs. 3c and d). Moreover, the operator $\langle S^2 \rangle_{\gamma}$ for different orbitals are all less than $3/4$, in agreement with the anticipated metallic nature of this state, as shown in Fig. 3e. Finally, for the benefit of the readers, note that the intuitive origin of the AFM2 “block” patterns has been clarified in previous literature and will not be repeated here. Essentially, in extended phase diagrams varying the electronic density, the block states arise as a compromise between fully FM and staggered AFM1 states, i.e., between FM vs AFM tendencies. Interested readers are referred to refs. 43,44. For the readers to better understand those phase transitions, we also show the spin structure $S(q)$ at $q = 0, \pi/2$, and π , corresponding to the FM, AFM2, and AFM1 phases, respectively, as a function of Δ_2 , as displayed in Fig. 3f.

The projected density of states (PDOS) ρ_{γ} at $U/W = 1.6$. To better understand the many different phases at intermediate electronic correlation, we calculated the orbital-resolved projected density of states $\rho_{\gamma}(\omega)$ vs frequency ω by using the dynamical DMRG, where the dynamical correlation vectors were obtained using the Krylov-space approach^{45,46}. A broadening parameter $\eta = 0.1$ was chosen in our DMRG calculations, as in previous cases. The chemical potential is obtained from $\mu = (E_{N+1} - E_{N-1})/2$, where E_N is the ground state energy of the N -particle system. $\rho_{\gamma}(\omega)$ is calculated from the portions of the spectra below and above μ , respectively, using:

$$\rho_{\gamma}(q, \omega < \mu) = \frac{1}{\pi} \text{Im} \left[\left\langle \Psi_0 \left| c_{i,\gamma}^{\dagger} \frac{1}{\omega + H - E_g + i\eta} c_{i,\gamma} \right| \Psi_0 \right\rangle \right], \quad (5)$$

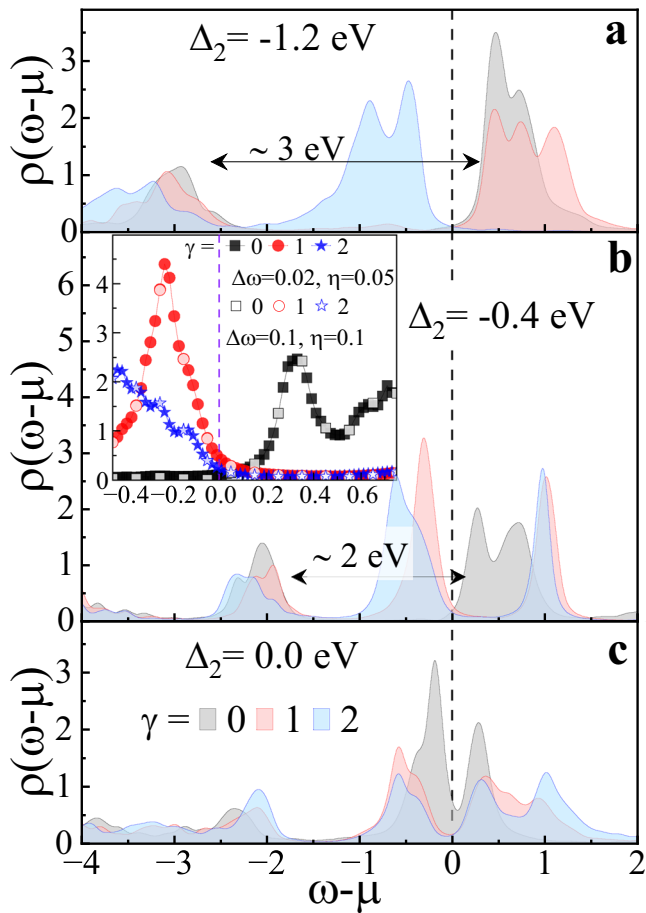


Fig. 4 Orbital-resolved density of states. Density of states (DOS) $\rho_\gamma(\omega)$ of different orbitals for different values of Δ_2 , at $U/W = 1.6$ and $J_H/U = 0.25$. **a** Antiferromagnetic1 Mott insulator (AFM1 MI) state at $\Delta_2 = -1.2$ eV. **b** Ferromagnetic orbital-selective Mott phase (FM OSMP) phase at $\Delta_2 = -0.4$ eV. **c** Antiferromagnetic2 metal (AFM2 M) state at $\Delta_2 = 0.0$ eV. $\Delta\omega = 0.1$ eV and broadening parameter $\eta = 0.1$ eV were chosen in our DMRG calculations. The black dash line represents chemical potential μ , which is calculated by using $\mu = (E_{N+1} - E_{N-1})/2$. For the inset in (b), smaller parameters $\Delta\omega = 0.02$ eV and $\eta = 0.05$ eV were used to calculate the DOS around the Fermi energy for comparison. The results indicate that the DOS is independent of the broadening parameter η . The purple dashed line represents the chemical potential μ , which is calculated by integrating the density of states for all ω 's to count the number of electrons.

$$\rho_\gamma(q, \omega > \mu) = \frac{-1}{\pi} \text{Im} \left[\left\langle \psi_0 \left| c_{i,\gamma} \frac{1}{\omega - H + E_g + i\eta} c_{i,\gamma}^\dagger \right| \psi_0 \right\rangle \right], \quad (6)$$

$$\rho_\gamma(\omega) = \rho_\gamma(q, \omega < \mu) + \rho_\gamma(q, \omega > \mu), \quad (7)$$

with ψ_0 as the ground state.

As displayed in Fig. 4, we calculated $\rho_\gamma(\omega)$ for several Δ_2 's, corresponding to different phases, at $J_H/U = 0.25$ and $U/W = 1.6$. At $\Delta_2 = -1.2$ eV, the $\gamma = 0$ and $\gamma = 1$ orbitals display a localized behavior with a Mott gap, while $\gamma = 2$ shows fully occupied characteristics below the chemical potential μ , Fig. 4a. Hence, this is a MI state, in agreement with previous discussions based on the site-average occupancy and charge fluctuations for this region.

At $\Delta_2 = -0.4$ eV, the $\gamma = 0$ orbital displays localized behavior with a Mott gap. Meanwhile, the $\gamma = 1$ and $\gamma = 2$ orbitals have electronic states crossing the Fermi level, leading to metallic

behavior, see Fig. 4b. Hence, the coexistence of localized and itinerant carriers supports the OSMP picture. By considering the spin-spin correlations $S(r)$ and spin structure factor $S(q)$, this state is an FM OSMP. In addition, the OSMP character is clear in our present work, supported by the results of charge occupation number and spin squared $\langle S^2 \rangle_\gamma$: a half-filled $\gamma = 0$ orbital does not have any charge or magnetic fluctuations while the $\gamma = 1$ and $\gamma = 2$ orbitals have non-integer numbers with sizeable charge and magnetic fluctuations (Fig. 3c-e). In fact, the hole-doped manganites are also an FM OSMP system, with t_{2g} orbitals localized and e_g metallic⁴⁷. In doped manganites, FM is induced by the double exchange mechanism⁴⁸, where off-diagonal hopping between the half and empty e_g orbitals plays an important role, similar to the half-full hopping discussed here.

Because of the small weight of the DOS for the orbitals 1 and 2 when crossing the Fermi level (Fig. 4b), an insulating tendency can not be fully excluded. Then, we also calculated the DOS around the Fermi energy with smaller parameters $\Delta\omega = 0.02$ eV and $\eta = 0.05$ eV to confirm our results. In this case, no obvious difference with the previous results was found, as shown in the inset in Fig. 4b, indicating that the value of the broadening is not a problem. In addition, the chemical potential is shown in the inset of Fig. 4b. μ is obtained by integrating the density of states in ω from the far left to a value that matches the total number of electrons expected. Note that the calculated chemical potential μ has an error bar of about ± 0.05 eV due to the grid used in the horizontal axis. At the Fermi level, the weight of $\gamma = 0$ orbital is virtually zero, while the $\gamma = 1$ and $\gamma = 2$ orbitals have small but non-zero weights, suggesting a clear difference between the three orbitals. In principle, if we have a dense enough ω , we could obtain more accurate μ by counting better the total occupied number of electrons. However, due to the very high cost of DMRG, we cannot have a very dense grid of ω to obtain $\rho(\omega)$ and μ with higher accuracy. Nevertheless, within these caveats, the results indicate that the DOS is independent of the broadening parameter η .

Furthermore, we also used the formula as defined in ref. ⁴⁹ to measure the gap as $E(N+1) + E(N-1) - 2E(N) = -0.00098$ eV which is basically zero, indicating that this is a metallic phase. We alert the readers that previous work by some members of this collaboration for another model observed orbital order and an insulating behavior with a small gap when the magnetic order is FM in the OSMP regime⁴⁹. Note that we can not exclude such a possibility that the system is in a non-orbital-selective insulating state with a very small gap, beyond our numerical accuracy. Here, we can only claim with certainty that in the present work with the grid of ω points used and with our measurement of orbital order correlations, and our measurement of the gap, we do not observe indications of orbital order and of a finite gap at the Fermi level. On the other hand, considering the small values of the DOS for orbitals 1 and 2, it is likely that nearby in parameter space an orbital-ordered insulating state could be stabilized. Searching for this phase is left for future efforts. Figure 4c clearly shows that all three orbitals are metallic with some electronic bands crossing μ , indicating itinerant electronic behavior, leading to an orbitally metallic state. This AFM2 metal was also predicted in the iron selenide chain based on the same model, where the crystal-field splitting Δ between half-filled and fully occupied orbitals is also small⁵⁰.

Strong U/W region. By increasing further the electronic correlation strength, the OSMP itinerant orbitals would become fully Mott-localized by the Hubbard strength U , resulting in a MI phase. To better understand the crystal-field effects on the FM MI

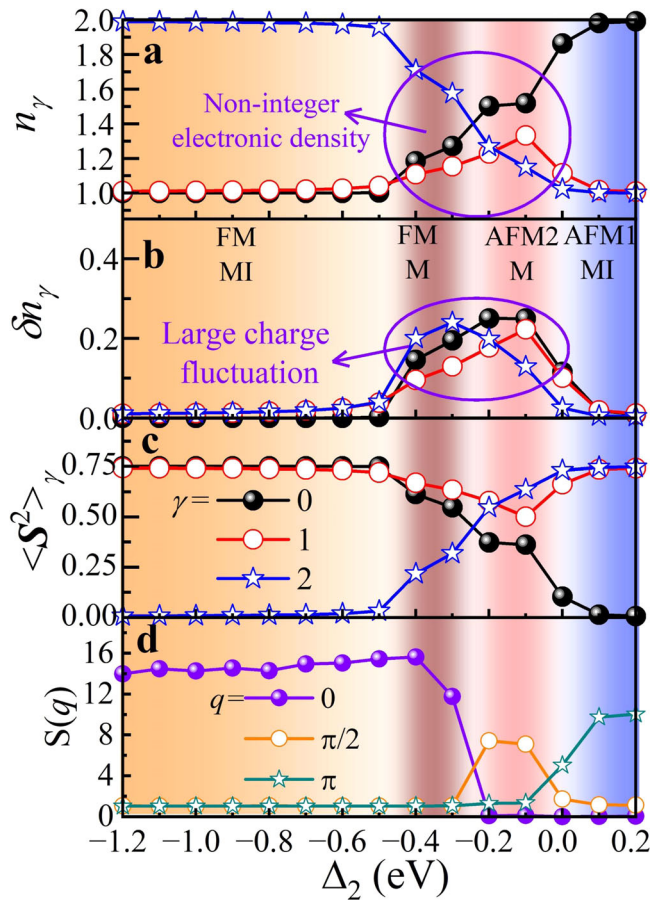


Fig. 5 Observables at strong correlation. **a** Orbital-resolved occupation number n_γ , **b** charge fluctuations $\delta n_\gamma = \frac{1}{L} \sum_i ((n_{i,\gamma}^2) - \langle n_{i,\gamma} \rangle^2)$, and **c** averaged value of the total spin-squared $\langle S^2 \rangle$, as a function of Δ_2 , at $J_{\parallel}/U = 0.25$ and $U/W = 8$. **d** The spin structure $S(q)$ at $q = 0, \pi/2$, and π as a function of Δ_2 . **a–d** Different electronic and magnetic phases are indicated by solid regions and labels, including ferromagnetic Mott insulator (FM MI, in yellow), ferromagnetic metal (FM M, in maroon), antiferromagnetic2 metal (AFM2 M, in pink), and antiferromagnetic1 Mott insulator (AFM1 MI, in purple). Here, the length of the chain is $L = 16$ and DMRG was used.

state, we will focus on the discussion of the main results for different values of Δ_2 at strong electronic correlation $U/W = 8$ in the phase diagram.

The FM MI state is found to dominate in a large region of Δ_2 , as shown in Fig. 5. When $\Delta_2 \lesssim -0.5$ eV, the $\gamma = 0$ and $\gamma = 1$ are half-filled ($n_0 = 1$ and $n_1 = 1$) and $\gamma = 2$ is a fully occupied orbital ($n_2 = 2$) without any charge fluctuation, as shown in Fig. 5a, b. Meanwhile, $\langle S^2 \rangle_0$ and $\langle S^2 \rangle_1$ are fixed at $3/4$, while $\langle S^2 \rangle_2$ is zero, indicating a strong Mott-localized behavior, as shown in Fig. 5c. Furthermore, the critical Hubbard U for the metal-insulator transition of the FM phase decreases as the crystal-field splitting $\Delta = \Delta_1 - \Delta_2$ (between doubly occupied and half-filled orbitals) increases. In this case, the FM MI state becomes more stable with larger crystal-field splitting Δ .

By increasing the crystal field Δ_2 , the system has non-integer electronic density n_γ in the three orbitals, see Fig. 5a, while the charge fluctuations δn_γ are large, leading to a metallic phase. In particular, when Δ_2 is in the region, closer to $\Delta_0 = -0.277$ eV and $\Delta_1 = -0.203$ eV, the competition between orbitals is the strongest. When $\Delta_2 \gtrsim 0.0$ eV, the three orbitals begin to localize with integer electronic density n_γ without charge fluctuations, leading to a MI state, as shown in Fig. 5b, c. In addition, the $\gamma = 0$ orbital becomes doubly occupied ($n_0 = 2$), while the $\gamma = 1$ and

$\gamma = 2$ orbitals are half-filled ($n_1 = 1$ and $n_2 = 1$). Furthermore, we also present the spin structure $S(q)$ at $q = 0, \pi/2$, and π , corresponding to the FM, AFM2, and AFM1 phases, respectively, for different values of Δ_2 to help the readers better understand the phase transitions, as shown in Fig. 5d. More details about spin-spin correlation and spin structure factor is shown in Supplementary Note VI.

Discussion

In multi-orbital systems with more than half-filled orbitals, it was recently shown that the *interorbital* hopping between half-filled and fully occupied orbitals can lead to an FM insulating phase³⁹. To understand how this *interorbital* hopping driven FM mechanism is affected by the crystal-field splitting $\Delta = \Delta_1 - \Delta_2$ between half-filled and fully occupied orbitals, as well as by the strength of the Hubbard repulsion U/W , here we comprehensively studied the Δ_2 vs U/W phase diagram of a three-orbital lattice model defined on a chain, by using DMRG many-body techniques. By modifying the value of Δ_2 over a broad range, the FM phase was found to be quite stable in the phase diagram, showing that the results of our previous study are not fragile, but indicative of robust tendencies, which also apply in higher dimensions. The FM state was found to display both FM OSMP or FM MI behavior, at intermediate or strong electronic correlations, respectively. In addition, several additional magnetic electronic phases were also revealed in our phase diagram arising from the competition of hoppings, crystal fields, and electronic correlations, involving AFM2 M, FM M, and AFM1 MI states.

Our results indicate that the FM order induced by this half-filled mechanism should be robust. This FM mechanism may explain the FM order in some other materials besides the one we studied before, such as in iron chains with d^6 configuration^{51–53}, one-dimensional $S = 1$ Ni-based chains⁵⁴, and Fe_3GeTe_2 ⁵⁵, where their unique lattice geometry provides the possibility of strong overlap between half-filled and fully occupied orbitals, thus creating a robust value for the interorbital coupling. On the other hand, it must be kept in mind that the intra-orbital hoppings (t_{11} and t_{22}) lead to AFM tendencies, thus a competition of tendencies will produce the final outcome. What other phases can be obtained by increasing the values of those inter-orbital hoppings in the large intra-orbital hopping case, as well as for different electronic correlations remains to be investigated (especially the evolution of the FM OSMP state).

Our study not only focuses on insulators but also on OSMP metals. Because in our case the hopping t_{11} (between $\gamma = 1$ orbitals) is much smaller than others, the $\gamma = 1$ orbitals could easily be localized while the other two orbitals still remain metallic in the intermediate correlated region, leading to the FM OSMP. Recently, a FM OSMP was reported in the Fe_3GeTe_2 system by neutron experiments⁵⁶. A more detailed study for the Fe_3GeTe_2 system would be interesting to perform. Furthermore, in iron-based superconductors, the OSMP is believed by some groups to play a key role to understand superconductivity^{13,57,58}. Hence, the next step is naturally to try to find additional real materials with the FM OSMP state to study whether superconductivity can be found in that state, complementing our search for FM insulators based on the *interorbital* hopping mechanism here discussed.

All these future directions of research require systematic work based on density functional theory (to calculate hopping and crystal fields and to identify the relevant orbitals) plus model calculations for correlations. Our study indicates the half-full mechanism could lead to robust FM order under effects of crystal-field splitting. Furthermore, AFM2 M and AFM1 MI phases were also found in our DMRG study at intermediate or strong Hubbard strengths,

where those phases were also found or predicted in some other iron chain systems with the same electronic density. Our work is a natural starting point for a variety of future studies to realize, both in theory and experiment, the important role of inter-hopping between half-filled and full occupied orbitals. This area of research has been barely touched until now.

Recently, the stability of the OSMF state with respect to the addition of interorbital hoppings was discussed by using the single-site dynamical mean-field theory but without including magnetism at zero and finite temperature⁵⁹. The next step would be interesting to study this matter related to finite temperature by including magnetism in more detail in future DMRG investigations.

In order to find new strong FM insulating states experimentalists should focus on materials with large orbital entanglement and strong crystal-field splitting between half-filled and fully occupied orbitals. The FM OSMF also can be obtained in a range of appropriate crystal field splittings, as in our calculations. Furthermore, crystal field splitting sensitively depends on chemical bonds and crystal structures, which could be in practice tuned by strain or pressure^{60,61}.

Methods

DMRG method. The model Hamiltonian discussed here was studied by using the DMRG method^{62,63}, where the DMRG++ computer package was employed⁶⁴. In our DMRG calculations, we used an $L = 16$ sites cluster chain geometry with open-boundary conditions. In addition, the electronic filling $n = 4$ in the three orbitals was considered. Furthermore, at least 1200 states were kept during our DMRG calculations and up to 21 sweeps were performed during the finite-size algorithm evolution. Truncation error remains below 10^{-6} for all of our results. An example input file and additional details can be found in Supplementary Note I. Note that all the DMRG calculations are performed at zero temperature $T = 0$. Size effect is discussed in Supplementary Note V.

The kinetic part of the Hamiltonian. The hopping matrix for the three-orbital chain system is defined³⁹ in orbital space as follows:

$$t_{\gamma\gamma'} = \begin{bmatrix} 0.187 & -0.054 & 0.020 \\ 0.054 & 0.351 & -0.349 \\ 0.020 & 0.349 & -0.433 \end{bmatrix}. \quad (8)$$

The crystal field splitting of the two orbitals are fixed as $\Delta_0 = -0.277$ and $\Delta_1 = -0.203$ eV, while Δ_2 was allowed to vary in our DMRG calculations. The total kinetic energy bandwidth W is 2.085 eV. All parameters mentioned above, involving the hopping matrix and crystal fields, were extracted from our previous work³⁹.

Observables. To obtain the phase diagram of the three-orbital 1D Hubbard model varying U/W and Δ_2 , several observables were measured using the DMRG many-body technique.

The spin-spin correlation is defined as:

$$S_{i,j} = \langle \mathbf{S}_i \cdot \mathbf{S}_j \rangle, \quad (9)$$

where $\mathbf{S}_i = \sum_{\gamma} \mathbf{S}_{i,\gamma}$.

The corresponding structure factor for spin is:

$$S(q) = \frac{1}{L} \sum_{j,k} e^{-iq(j-k)} \langle \mathbf{S}_k \cdot \mathbf{S}_j \rangle, \quad (10)$$

The site-average occupancy of orbitals is:

$$n_{\gamma} = \frac{1}{L} \langle n_{\gamma\sigma} \rangle. \quad (11)$$

The orbital-resolved charge fluctuation is defined as:

$$\delta n_{\gamma} = \frac{1}{L} \sum_i \langle (n_{\gamma,i}^2) - (n_{\gamma,i})^2 \rangle. \quad (12)$$

The mean value of the squared spin for each orbital is defined as:

$$\langle \mathbf{S}^2 \rangle_{\gamma} = \frac{1}{L} \sum_i \langle \mathbf{S}_{i,\gamma} \cdot \mathbf{S}_{i,\gamma} \rangle. \quad (13)$$

Data availability

The data that support the findings of this study are available from the corresponding author upon request.

Code availability

The computer codes used in this study are available at <https://g1257.github.io/dmrgPlusPlus/>.

Received: 9 March 2023; Accepted: 20 July 2023;

Published online: 04 August 2023

References

- Dagotto, E. Correlated electrons in high-temperature superconductors. *Rev. Mod. Phys.* **66**, 763 (1994).
- Scalapino, D. J. A common thread: the pairing interaction for unconventional superconductors. *Rev. Mod. Phys.* **84**, 1383 (2012).
- Dai, P. C., Hu, J. P. & Dagotto, E. Magnetism and its microscopic origin in iron-based high-temperature superconductors. *Nat. Phys.* **8**, 709–718 (2012).
- Dagotto, E. The unexpected properties of alkali metal iron selenide superconductors. *Rev. Mod. Phys.* **85**, 849 (2013).
- Khomskii, I. K. & Streltsov, S. V. Orbital effects in solids: basics, recent progress, and opportunities. *Chem. Rev.* **121**, 2992–3030 (2022).
- Zhang, Y., Lin, L.-F., Moreo, A. & Dagotto, E. $J = 0$ nonmagnetic insulating state in K_2OsX_6 ($X = \text{F, Cl, Br}$). *Phys. Rev. B* **106**, 155148 (2022).
- Streltsov, S. V. & Khomskii, D. I. Orbital-dependent singlet dimers and orbital-selective peierls transitions in transition-metal compounds. *Phys. Rev. B* **89**, 161112 (2014).
- Zhang, Y., Lin, L.-F., Moreo, A., Alvarez, G. & Dagotto, E. Peierls transition, ferroelectricity, and spin-singlet formation in monolayer VOI_2 . *Phys. Rev. B* **103**, L121114 (2021).
- Tokura, Y. & Nagaosa, N. Orbital physics in transition-metal oxides. *Science* **288**, 462–468 (2000).
- Lin, L.-F., Kaushal, N., Zhang, Y., Moreo, A. & Dagotto, E. Orbital ordering in the layered perovskite material CsVF_4 . *Phys. Rev. Mater.* **5**, 025001 (2021).
- Caron, J. M. et al. Orbital-selective magnetism in the spin-ladder iron selenides $\text{Ba}_{1-x}\text{K}_x\text{Fe}_2\text{Se}_3$. *Phys. Rev. B* **85**, 180405(R) (2012).
- Zhang, Y., Lin, L.-F., Moreo, A. & Dagotto, E. Orbital-selective peierls phase in the metallic dimerized chain MoOCl_2 . *Phys. Rev. B* **104**, L060102 (2021).
- Yin, Z. P., Haule, K. & Kotliar, G. Kinetic frustration and the nature of the magnetic and paramagnetic states in iron pnictides and iron chalcogenides. *Nat. Mater.* **10**, 932–935 (2011).
- Kostin, A. et al. Imaging orbital-selective quasiparticles in the hund s metal state of FeSe . *Nat. Mater.* **17**, 869–874 (2018).
- Zhang, Y., Lin, L.-F., Alvarez, G., Moreo, A. & Dagotto, E. Magnetic states of quasi-one-dimensional iron chalcogenide Ba_2FeS_3 . *Phys. Rev. B* **104**, 125122 (2021).
- Di Capua, R. et al. Orbital selective switching of ferromagnetism in an oxide quasi two-dimensional electron gas. *npj Quantum Mater.* **7**, 24 (2022).
- de'Medici, L., Giovannetti, G. & Capone, M. Selective mott physics as a key to iron superconductors. *Phys. Rev. Lett.* **112**, 177001 (2014).
- Mourigal, M. et al. Block magnetic excitations in the orbitally selective mott insulator BaFe_2Se_3 . *Phys. Rev. Lett.* **115**, 047401 (2015).
- Craco, L. & Leoni, S. Pressure-induced orbital-selective metal from the mott insulator BaFe_2Se_3 . *Phys. Rev. B* **101**, 245133 (2020).
- Lin, L.-F. et al. Prediction of orbital-selective mott phases and block magnetic states in the quasi-one-dimensional iron chain $\text{Ce}_2\text{O}_2\text{FeSe}_2$ under hole and electron doping. *Phys. Rev. B* **105**, 075119 (2022).
- Stepanov, E. A. Eliminating orbital selectivity from the metal-insulator transition by strong magnetic fluctuations. *Phys. Rev. Lett.* **129**, 096404 (2022).
- Žutić, I., Fabian, J. & Sarma, S. D. Spintronics: fundamentals and applications. *Rev. Mod. Phys.* **76**, 323 (2004).
- Dieny, B. Opportunities and challenges for spintronics in the microelectronics industry. *Nat. Electron.* **3**, 446–459 (2020).
- Ahn, E. C. 2D materials for spintronic devices. *npj 2D Mater. Appl.* **4**, 17 (2020).
- Choi, W. S., Kang, K. T., Jeon, H., Gai, Z. & Lee, H. N. Highly insulating ferromagnetic cobaltite heterostructures. *Curr. Appl. Phys.* **17**, 722–726 (2017).
- Frantti, J. et al. In quest of a ferromagnetic insulator: Structure-controlled magnetism in Mg-Ti-O thin films. *J. Phys. Chem. C* **123**, 19970–19978 (2019).
- Tsurkan, V., Von Nidda, H.-A. K., Deisenhofer, J., Lunkenheimer, P. & Loidl, A. On the complexity of spinels: Magnetic, electronic, and polar ground states. *Phys. Rep.* **926**, 1–86 (2021).
- Emori, S. & Li, P. Ferrimagnetic insulators for spintronics: beyond garnets. *J. Appl. Phys.* **129**, 020901, (2021).
- Tsubokawa, I. On the magnetic properties of a CrBr_3 single crystal. *J. Phys. Soc. Jpn.* **15**, 1664–1668 (1960).
- Zhong, D. et al. Van der waals engineering of ferromagnetic semiconductor heterostructures for spin and valleytronics. *Sci. Adv.* **3**, e1603113 (2017).

31. Lohmann, M. et al. Probing magnetism in insulating $\text{Cr}_2\text{Ge}_2\text{Te}_6$ by induced anomalous hall effect in Pt. *Nano Lett.* **19**, 2397–2403 (2019).
32. Schmehl, A. et al. Epitaxial integration of the highly spin-polarized ferromagnetic semiconductor EuO with silicon and GaN. *Nat. Mater.* **6**, 882–887 (2007).
33. Wei, P. et al. Strong interfacial exchange field in the graphene/EuS heterostructure. *Nat. Mater.* **15**, 711–716 (2016).
34. Isasa, M. et al. Spin hall magnetoresistance at Pt/CoFe₂O₄ interfaces and texture effects. *Appl. Phys. Lett.* **105**, 142402 (2014).
35. Amamou, W. et al. Magnetic proximity effect in Pt/CoFe₂O₄ bilayers. *Phys. Rev. Mater.* **2**, 011401(R) (2018).
36. Lehmann, H. & Robbins, M. Electrical transport properties of the insulating ferromagnetic spinels CdCr₂S₄ and CdCr₂Se₄. *J. Appl. Phys.* **37**, 1389 (1966).
37. Anderson, P. W. New approach to the theory of superexchange interactions. *Phys. Rev.* **115**, 2 (1959).
38. Goodenough, J. B. *Magnetism and the Chemical Bond* (Wiley Interscience, New York, 1963).
39. Lin, L.-F., Zhang, Y., Alvarez, G., Moreo, A. & Dagotto, E. Origin of insulating ferromagnetism in iron oxychalcogenide Ce₂O₂FeSe₂. *Phys. Rev. Lett.* **127**, 077204 (2021).
40. McCabe, E. E., Free, D. G. & Evans, J. S. A new iron oxyarsenide Ce₂O₂FeAs₂: synthesis and characterisation. *Chem. Commun.* **47**, 1261–1263 (2011).
41. McCabe, E. E., Stock, C., Bettis, J. L., Whangbo, M. H. & Evans, J. S. O. Magnetism of the Fe²⁺ and Ce³⁺ sublattices in Ce₂O₂FeSe₂: a combined neutron powder diffraction, inelastic neutron scattering, and density functional study. *Phys. Rev. B* **90**, 235115 (2014).
42. Mostofi, A. A. et al. Wannier90: a tool for obtaining maximally-localised wannier functions. *Comput. Phys. Commun.* **178**, 685–699 (2008).
43. Herbrich, J. et al. Novel magnetic block states in low-dimensional iron-based superconductors. *Phys. Rev. Lett.* **123**, 027203 (2019).
44. Sroda, M. et al. Quantum magnetism of iron-based ladders: blocks, spirals, and spin flux. *Phys. Rev. B* **104**, 045128 (2021).
45. Kühner, T. D. & White, S. R. Dynamical correlation functions using the density matrix renormalization group. *Phys. Rev. B* **60**, 335 (1999).
46. Nocera, A. & Alvarez, G. Spectral functions with the density matrix renormalization group: Krylov-space approach for correction vectors. *Phys. Rev. E* **94**, 053308 (2016).
47. Şen, C. & Dagotto, E. Properties of La_{0.7}Ca_{0.3}MnO₃ under extreme tensile strain. *Phys. Rev. B* **102**, 035126 (2020).
48. Dagotto, E., Hotta, T. & Moreo, A. Colossal magnetoresistant materials: the key role of phase separation. *Phys. Rep.* **344**, 1–153 (2001).
49. Li, S. et al. Nonlocal correlations in the orbital selective Mott phase of a one-dimensional multiorbital Hubbard model. *Phys. Rev. B* **94**, 235126 (2016).
50. Pandey, B. et al. Prediction of exotic magnetic states in the alkali metal quasi-one-dimensional iron selenide compound Na₂FeSe₂. *Phys. Rev. B* **102**, 035149 (2020).
51. Eibschütz, M., Lines, M. & Sherwood, R. Magnetism in orbitally unquenched chainar compounds. II. the ferromagnetic case: RbFeCl₃. *Phys. Rev. B* **11**, 4595 (1975).
52. Toda, M. et al. Field-induced magnetic order in the singlet-ground-state magnet CsFeCl₃. *Phys. Rev. B* **71**, 224426 (2005).
53. Stüble, P., Peschke, S., Johrendt, D. & Röhr, C. Na₇[Fe₂S₆], Na₂[Fe₂S₂] and Na₂[Fe₂Se₂]: new reduced sodium chalcogenido ferrates. *J. Solid State Chem.* **258**, 416–430 (2018).
54. Kjems, J. & Steiner, M. Evidence for soliton modes in the one-dimensional ferromagnet CsNiF₃. *Phys. Rev. Lett.* **41**, 1137 (1978).
55. Deng, Y. et al. Gate-tunable room-temperature ferromagnetism in two-dimensional Fe₃GeTe₂. *Nature* **563**, 94–99 (2018).
56. Bai, X. et al. Antiferromagnetic fluctuations and orbital-selective mott transition in the van der waals ferromagnet Fe_{3-x}GeTe₂. *Phys. Rev. B* **106**, L180409 (2022).
57. Yi, M. et al. Observation of temperature-induced crossover to an orbital-selective mott phase in A_xFe_{2-y}Se₂ (A =K, Rb) superconductors. *Phys. Rev. Lett.* **110**, 067003 (2013).
58. Yu, R. & Si, Q. Orbital-selective mott phase in multiorbital models for alkaline iron selenides K_{1-x}Fe_{2-y}Se₂. *Phys. Rev. Lett.* **110**, 146402 (2013).
59. Kugler, F. B. & Kotliar, G. Is the Orbital-Selective Mott Phase Stable against Interorbital Hopping? *Phys. Rev. Lett.* **129**, 096403 (2022).
60. Liang, A. et al. High-pressure tuning of *d* – *d* crystal-field electronic transitions and electronic band gap in Co(IO₃)₂. *Phys. Rev. B* **105**, 115204 (2022).
61. Byrne, P. J. et al. Piezochromism in nickel salicylaloximato complexes: tuning crystal-field splitting with high pressure. *Chem. Eur. J.* **18**, 7738–7748 (2012).
62. White, S. R. Density matrix formulation for quantum renormalization groups. *Phys. Rev. Lett.* **69**, 2863 (1992).
63. Schollwöck, U. The density-matrix renormalization group. *Rev. Mod. Phys.* **77**, 259 (2005).
64. Alvarez, G. The density matrix renormalization group for strongly correlated electron systems: a generic implementation. *Comput. Phys. Commun.* **180**, 1572–1578 (2009).
65. Momma, K. & Izumi, F. Vesta 3 for three-dimensional visualization of crystal, volumetric and morphology data. *J. Appl. Crystallogr.* **44**, 1272–1276 (2011).

Acknowledgements

The work of L.-F.L., Y.Z., M.A.M., A.F.M., A.M., and E.D. was supported by the U.S. Department of Energy (DOE), Office of Science, Basic Energy Sciences (BES), Materials Sciences and Engineering Division. The work of G. A. was supported by the U.S. Department of Energy, Office of Science, National Quantum Information Science Research Centers, Quantum Science Center.

Author contributions

L.L., Y.Z., and E.D. designed the project. L.L. carried out numerical calculations for the multiorbital Hubbard model. G.A. developed the DMRG++ computer program. L.L., Y.Z., M.A.M., A.F.M., A.M., and E.D. wrote the manuscript. All co-authors provided useful comments and discussion on the paper.

Competing interests

The authors declare no competing interests.

Additional information

Supplementary information The online version contains supplementary material available at <https://doi.org/10.1038/s42005-023-01314-w>.

Correspondence and requests for materials should be addressed to Ling-Fang Lin or Yang Zhang.

Peer review information *Communications Physics* thanks the anonymous reviewers for their contribution to the peer review of this work. A peer review file is available.

Reprints and permission information is available at <http://www.nature.com/reprints>

Publisher's note Springer Nature remains neutral with regard to jurisdictional claims in published maps and institutional affiliations.



Open Access This article is licensed under a Creative Commons Attribution 4.0 International License, which permits use, sharing, adaptation, distribution and reproduction in any medium or format, as long as you give appropriate credit to the original author(s) and the source, provide a link to the Creative Commons license, and indicate if changes were made. The images or other third party material in this article are included in the article's Creative Commons license, unless indicated otherwise in a credit line to the material. If material is not included in the article's Creative Commons license and your intended use is not permitted by statutory regulation or exceeds the permitted use, you will need to obtain permission directly from the copyright holder. To view a copy of this license, visit <http://creativecommons.org/licenses/by/4.0/>.

© The Author(s) 2023